

Vibration of Soft, Twisted Beams for Under-Actuated Quadrupedal Locomotion*

Yuhao Jiang¹, Fuchen Chen², Jamie Paik¹, and Daniel M. Aukes²

Abstract—Under-actuated compliant robotic systems offer a promising approach to mitigating actuation and control challenges by harnessing pre-designed, embodied dynamic behaviors. This paper presents Flix-Walker, a novel, untethered, centimeter-scale quadrupedal robot inspired by compliant under-actuated mechanisms. Flix-Walker employs flexible, helix-shaped beams as legs, which are actuated by vibrations from just two motors to achieve three distinct mobility modes. We analyze the actuation parameters required to generate various locomotion modes through both simulation and prototype experiments. The effects of system and environmental variations on locomotion performance are examined, and we propose a generic metric for selecting control parameters that produce robust and functional motions. Experiments validate the effectiveness and robustness of these actuation parameters within a closed-loop control framework, demonstrating reliable trajectory-tracking and self-navigation capabilities.

Index Terms—Underactuated Robots, Compliant Joint Mechanism, Robotic Locomotion, Soft Robot Applications

I. INTRODUCTION

Under-actuated, compliant systems exploit structural dynamics to produce complex robotic motions for locomotion and manipulation, while reducing actuation demands. Leveraging these dynamic behaviors diminishes the need for active actuation, lowers controller complexity, reduces actuator count, and simplifies fabrication [1], [2]. Legged robots offer superior maneuverability in cluttered terrain compared to wheeled or tracked platforms [3], [4]. However, their reliance on intricate actuation and control typically results in larger size, higher power consumption, and increased fabrication costs, limiting their deployment in swarm robotics and confined spaces.

Modeling and understanding under-actuated systems, especially in the presence of impacts, friction, and environmental uncertainties, remains a significant challenge. In this study, we present Flix-Walker, an untethered, 350 g quadruped robot that achieves directional locomotion via a controllable vibrational source (Figure 1(a)). The robot employs soft, twisted beams with complex dynamics to achieve a number of effective locomotion degrees of freedom that exceeds its actuator count. To control this system, we introduce a paradigm called “Dynamics-based Demultiplexing.” In this framework, the planar vibrational force input, characterized by shaking frequency (f) and direction (θ), serves as a composite control signal

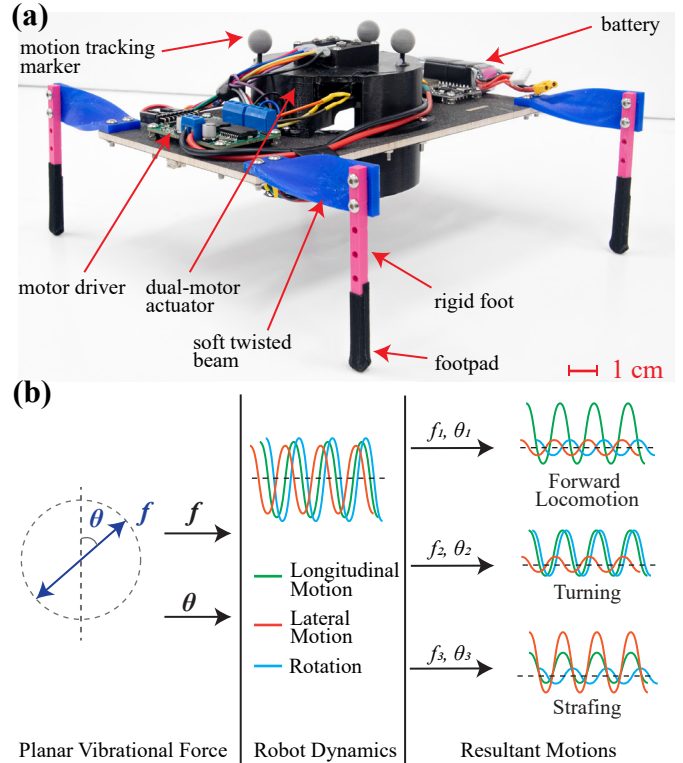


Fig. 1. **Flix-Walker.** (a) The Flix-Walker prototype; (b) the working principle of Flix-Walker: The vibration frequency (f) and direction (θ) act as selectors, while the robot’s intrinsic dynamics function as a demultiplexer, selectively expressing specific motion modes. By tuning f and θ , Flix-Walker can achieve three types of mobility: forward locomotion, turning, and strafing.

that excites the robot’s longitudinal, lateral, and rotational motion components (see Figure 1(b)). The vibration frequency and direction act as selectors, while the robot’s intrinsic dynamics function as a demultiplexer, selectively expressing and amplifying specific motion components. By fine-tuning these parameters, Flix-Walker can express various combinations of three distinct locomotion modes: linear translation, turning, and lateral strafing. This signal-processing-inspired approach provides a novel strategy for programmable gait generation, offering a powerful new paradigm for underactuated robotic mobility. While previous work explored the fundamental phenomenology of the soft twisted beams in a 1D constrained setup [5], this work advances to a holistic framework for controllable robotic synthesis. We introduce a dual-rotor actuation scheme that generates vectorable forces and torques to enable untethered, 3-DoF planar mobility, moving beyond the prior limitations. Furthermore, we formalize the control paradigm as “Dynamics-based Demultiplexing” and validate

*This work is supported by the National Science Foundation Grant No. 1935324. (Corresponding author: Daniel Aukes)

¹Y. Jiang and J. Paik are with the Reconfigurable Robotics Laboratory, School of Engineering, EPFL, Lausanne, 1015, Switzerland. {yuhao.jiang, jamie.paik}@epfl.ch

²F. Chen and D. M. Aukes were with The School of Manufacturing Systems and Networks, Fulton Schools of Engineering, Arizona State University, Mesa, AZ, 85212, USA. fchen65@asu.edu, danaukes@danaukes.com

it through rigorous model calibration, sensitivity analysis, and closed-loop trajectory tracking, demonstrating capabilities not previously realized.

To analyze the Flix-Walker’s dynamic behavior under various control inputs, we developed a dynamic model based on the pseudo-rigid-body method, which was implemented in the MuJoCo simulator [6] and calibrated to match the prototype’s performance. Through simulations, validated via experiments with the prototype, we have identified effective actuation parameters and examined the system’s sensitivity to system and environmental variation. These findings establish a robust framework for understanding the complex relationships guiding robot behavior and for selecting actuation parameters that are resilient to key sources of variation.

A. Background

Under-actuated compliant systems are increasingly prominent in soft robotics for reducing actuation and control requirements. Advances in metamaterials and mechanical structures have enabled soft robots to perform sensing [7], [8] and actuation [9], [10] tasks more efficiently, addressing key challenges in actuation and control. However, conventional soft robots, despite their adaptability and numerous degrees of freedom, usually require bulky actuators and complex controllers to achieve specific locomotion tasks [11], [12], complicating modeling, fabrication, and scalability.

Legged locomotion has advanced across a broad size range, from meter-scale [13], [14] to centimeter- and millimeter-scale robots [15], [16], [17]. While these robots can be highly maneuverable, most use more than ten actuators, increasing power, system complexity, and fabrication costs.

Underactuated locomotion strategies have been developed to minimize actuator count. Some designs use mechanical linkages or body curvature for predefined gaits, enabling high-speed movement with fewer actuators [18], [19]. Recent studies show that leveraging material properties and structural dynamics allows for effective locomotion with fewer actuators [20], [21], enabling simpler, scalable robots for swarm and exploration applications. However, these approaches often restrict robots to limited movement modes, typically linear translation or turning, reducing versatility.

In this context, we introduce Flix-Walker, a centimeter-scale (22 cm, 350 g) locomotor that combines dynamically-coupled compliant mechanisms with vibrational actuation. Driven by just two brushless motors and equipped with 3D-printed soft, twisted beams, Flix-Walker achieves three distinct mobility degrees of freedom: forward locomotion, turning, and strafing. This is enabled by dynamics-based demultiplexing, where different vibrational frequencies and directions (serving as selector signals) excite specific gait dynamics within the robot’s compliant structure (acting as a demultiplexer). As a result, Flix-Walker attains more mobility DoF than the number of actuators, while also simplifying manufacturing and reducing costs. To contextualize Flix-Walker’s performance, we compare its locomotion capabilities and body scale to those of other state-of-the-art vibration-driven locomotors (see Table I).

This study fits under the umbrella of a new class of devices termed Soft Curved Reconfigurable Anisotropic Mechanisms

TABLE I
COMPARISON WITH STATE-OF-THE-ART VIBRATION-DRIVEN LOCOMOTORS.

Work Index	Actuator Count	Capable Motions	Body Length (mm)	Body Mass (g)	Power Source
This Work	2	Forward locomotion, Turning, Strafing	220	350	Onboard
[26]	1	Forward locomotion	100	16.2	Onboard
[27]	1	Forward locomotion, Turning	20	0.0756	Onboard
[28]	1	Forward locomotion, Turning	25	1.2	Onboard
[29]	2	Forward locomotion, Turning	33	18	Onboard
[30]	2	Forward locomotion, Turning	40	5	Tethered
[31]	2	Forward locomotion, Turning	35	6	Onboard

(SCRAMs), previously explored in pinched tubes [22], [23], [24], buckling beams [2], [25], and twisted beams [5]. Leveraging the shape and material properties of soft structures allows complex actuation signals to be consolidated and simplified for generating complex motions.

B. Contributions

The contributions of this paper are summarized as follows:

- 1) This paper introduces a novel underactuated robotic locomotor that uses just two motors to generate vibrational forces, with soft twisted beam limbs enabling tunable dynamic locomotion.
- 2) This paper presents a revised Pseudo-Rigid Body Model (PRBM) with an optimization-based calibration process, permitting high-fidelity dynamic simulation of the compliant system in a rigid body simulator (MuJoCo).
- 3) This paper demonstrates how selecting different vibration inputs enables the robot’s intrinsic dynamics to act as a demultiplexer, producing distinct locomotion modes.
- 4) This paper investigates the impact of manufacturing variations and environmental disturbances on robot behavior through simulation and experiments. A generalized method is developed to select control parameters for underactuated compliant robots, balancing performance and robustness across various locomotion modes.

II. ROBOT DESIGN AND MODELING

This section presents the design and modeling of Flix-Walker, covering full-robot simulation, pseudo-rigid-body modeling of twisted beam legs, and the actuation system. It describes parameter identification for leg model calibration and uses simulation to analyze actuation dynamics and validate the design.

A. Robot Design and Prototyping

Flix-Walker comprises three primary components: 1) a lightweight, rigid carbon fiber body plate for efficient transmission of actuation forces; 2) four soft, twisted-beam legs

TABLE II
DESIGN PARAMETERS

Parameter	Symbol	Value	Parameter	Symbol	Value
Body plate length	L_{body}	220 mm	Foot length	L_{foot}	85 mm
Body plate width	W_{body}	120 mm	Foot width	W_{foot}	5 mm
Body plate thickness	T_{body}	3.5 mm	Rotor arm length	l	28 mm
Leg length	L_{leg}	50 mm	Rotor vertical distance	h	28 mm
Leg width	W_{leg}	20 mm	Rotor offset mass	m	12 g
Leg thickness	T_{leg}	3 mm	Leg twist angle	ϕ	90°

at the plate’s corners, each terminating in a rigid, 3D-printed PLA foot; and 3) a dual-rotor shaker at the body center, each rotor driven by its own brushless motor (YUNEEC 3S 450 KV BLDC), as described in Section II-E and shown in Figure 2(d).

- 1) Robot Body: The body is constructed from a 16 g CNC-machined, carbon fiber sandwich sheet (DragonPlate EconomyPlate Carbon Fiber Balsa Core, 3.5 mm thick). This design provides the necessary rigidity to transmit vibrational forces while minimizing mass and inertia.
- 2) Robot Legs: The legs are 3D printed in TPU95A, following the geometry from [5] with a 90° twist angle ϕ and $T_{\text{leg}} = 3$ mm thickness for effective locomotion. Key parameters are shown in Figure 2(c) and Table II.
- 3) Robot Prototype: The prototype (see Figure 1(a)) integrates an ESP32 microcontroller with SimpleFOC motor driver at the tail and a 300 mAh 3-cell Li-Po battery at the front for balance. The total weight is 350 g. Two brushless motors with offset rotary loads are mounted in the cage. Full specifications are listed in Table II.

B. Robot Modeling

The dynamic model of the Flix-Walker was developed for simulation in MuJoCo. This comprehensive model integrates a pseudo-rigid-body approach to represent the soft twisted beam design, alongside rigid components that match the physical prototype, as detailed in Section II-A. An overview of the resulting MuJoCo model is shown in Figure 2(b).

Due to the robot’s complexity, with four twisted beams and contact points, as well as two rotors, calibrating the model presents significant challenges, particularly given the large search space of the model’s parameters. Further complicating calibration, manufacturing and assembly inconsistencies in the physical prototype introduce additional sources of variability.

To improve model fidelity, a two-stage calibration process was implemented using reference data collected from prototype experiments. This process involves: 1) single leg identification, which establishes baseline stiffness and damping values for the soft twisted beam legs; and 2) full model calibration, which further tunes these baseline parameters and introduces variance factors to account for manufacturing differences.

C. Single Leg Identification

Pseudo-rigid body modeling (PRBM) [32] is employed to capture the dynamic behavior of the soft twisted beams due to its computational efficiency and compatibility with

rigid-body dynamics simulators such as MuJoCo. As shown in Figure 2(a), the beam is approximated by three equal-length, equal-mass rigid segments connected in series. The proximal segment is attached to the base through a single revolute joint. The remaining two segment-to-segment connections are modeled as joint modules that include a fixed offset rotation of $\phi_{\text{seg}} = 45^\circ$ about the local Y -axis of the child segment relative to its parent. Accordingly, the first segment is aligned with the base, while the second and third segments incorporate the ϕ_{seg} offset relative to their parent segment, yielding a cumulative 90° geometric twist between the first and last segments about the initial segment’s Y -axis.

At each of the two segment-to-segment connections, two orthogonal revolute joints are used: an X -axis joint to model bending and a Y -axis joint to model twisting. All bending joints share stiffness and damping parameters ($k_{\text{bend}}, b_{\text{bend}}$), and all twisting joints share ($k_{\text{twist}}, b_{\text{twist}}$), consistent with the beam’s constant geometry and material (UltiMaker TPU 95A). Joint stiffness scales with the beam’s flexural rigidity and inversely with segment length.

We identify the single-leg PRBM parameter set $S = \{k_{\text{bend}}, b_{\text{bend}}, k_{\text{twist}}, b_{\text{twist}}\}$ via simulation-based optimization; the procedure is summarized in Figure 2(f). Reference data are collected from laboratory tests on a soft twisted beam with the same dimensions as the robotic leg in Section II-A. In each trial, the beam is laterally deflected, a load is attached at the distal end, and the load is suddenly released; the distal-end motion during recovery is recorded. This protocol is repeated for three loading directions, with the load applied at -60° , 0° (vertical), and 60° . We replicate the same loading and unloading protocol in MuJoCo (Figure 2(e)) and record the simulated distal-end recovery motion.

Parameter fitting is performed using Bayesian hyperparameter optimization [33] to minimize an objective defined as the root mean square error (RMSE) between simulated and experimental position (P_i) and rotation (R_i) trajectories. The optimization problem is formulated as:

$$S^* = \arg \min_S \text{RMSE} \left([P_i(n), R_i(n)], [\hat{P}_i(n), \hat{R}_i(n)] \right), \quad (1)$$

where $S = \{k_{\text{bend}}, b_{\text{bend}}, k_{\text{twist}}, b_{\text{twist}}\}$, and $i \in \{x, y, z\}$ denotes the spatial axes; $P_i(n)$ and $R_i(n)$ are the simulated position and rotation at time step n along axis i , while $\hat{P}_i(n)$ and $\hat{R}_i(n)$ are the corresponding experimental reference data. The comparison between reference and model-fitted results is shown in Figure 3(a). The optimized parameter set $S^* = \{1.062072, 2.21209, 0.0024, 0.00183\}$.

D. Full Model Calibration

After identifying the single-leg model, we calibrate the full robot model to account for discrepancies introduced by manufacturing tolerances and assembly errors. The procedure is summarized in Figure 2(g). We introduce an error parameter set \mathbf{X} :

$$\mathbf{X} = \left\{ \delta_{k,\text{bend},i}, \delta_{b,\text{bend},i}, \delta_{k,\text{twist},i}, \delta_{b,\text{twist},i}, \mu_i, m_{\text{mag}}, m_x, m_y \right\}, \quad (2)$$

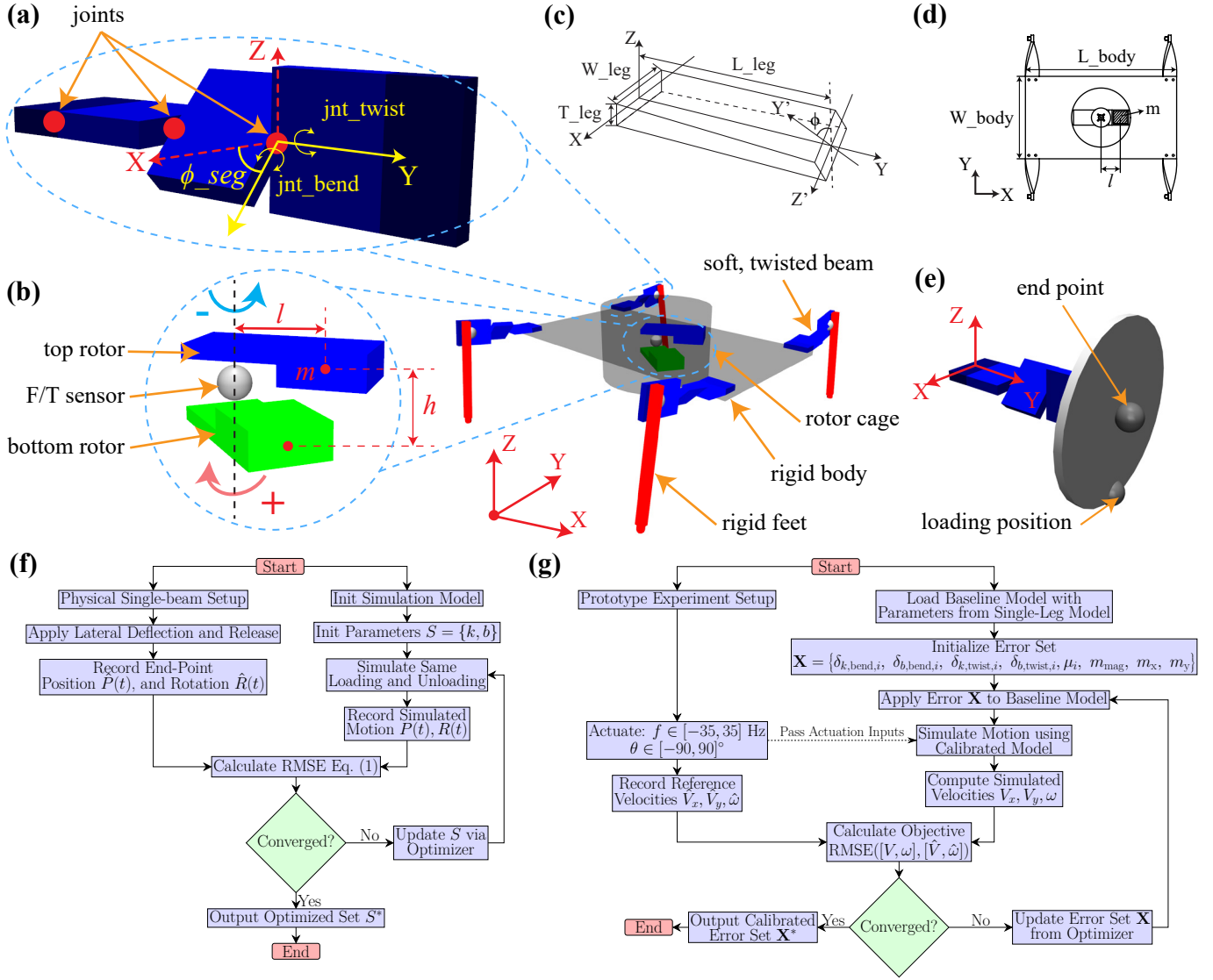


Fig. 2. **Modeling procedure and simulation setup of Flix-Walker.** (a) The pseudo-rigid-body model of the soft twisted beam. (b) The simulation model for the dual-rotor actuation system; (c) Design diagram of the soft twisted beam leg; (d) Design diagram of the robot body. (e) Simulation setup for calibrating the single-leg model. (f) The process for identifying parameters for the single-leg model. (g) The full model calibration process, where error terms are optimized by comparing prototype experiments with the baseline model simulation.

where $i \in \{\text{fl, fr, rl, rr}\}$. The parameters δ denote per-leg proportional errors in stiffness (k) and damping (b) relative to the baseline values identified in Section II-C (front-left, front-right, rear-left, and rear-right legs). To avoid bias from assumed contact parameters, the per-foot tangential friction coefficients μ_i are obtained from bench-top measurements on the test surface and incorporated into the full-model calibration. The remaining terms capture the body mass magnitude m_{mag} , and the body mass offsets (m_x, m_y) in the body frame.

We collect reference data from prototype experiments (see Section II-A and Figure 1(b)) by actuating the robot over driving frequencies $f \in [-35, 35]$ Hz and shaking orientations $\theta \in [-90, 90]^\circ$ for 8 s while recording its pose. The same command set is replayed in simulation to obtain corresponding pose/velocity trajectories.

We then use the same optimizer to fit \mathbf{X} by minimizing the discrepancy between simulated and experimental motions,

defined as the RMSE between the average linear velocities V_i in the longitudinal (x) and lateral (y) directions and the yaw rate ω about the z -axis:

$$\mathbf{X}^* = \arg \min_{\mathbf{X}} \text{RMSE} \left([V_i(n), \omega(n)], [\hat{V}_i(n), \hat{\omega}(n)] \right), \quad (3)$$

where $i \in \{x, y\}$ and n indexes time steps; $\hat{V}_i(n)$ and $\hat{\omega}(n)$ denote the experimental measurements. The resulting speed maps for the prototype and the calibrated simulation are shown in Figure 3(c), demonstrating close agreement and indicating that the calibrated model captures the robot's dynamics.

E. Actuation Analysis

Flix-Walker employs a dual-motor system to generate a unidirectional vibrational force, as illustrated in Figure 2(b). Two motors, each with an off-axis mass m mounted at an arm length l , are positioned at the center of the body and rotate in

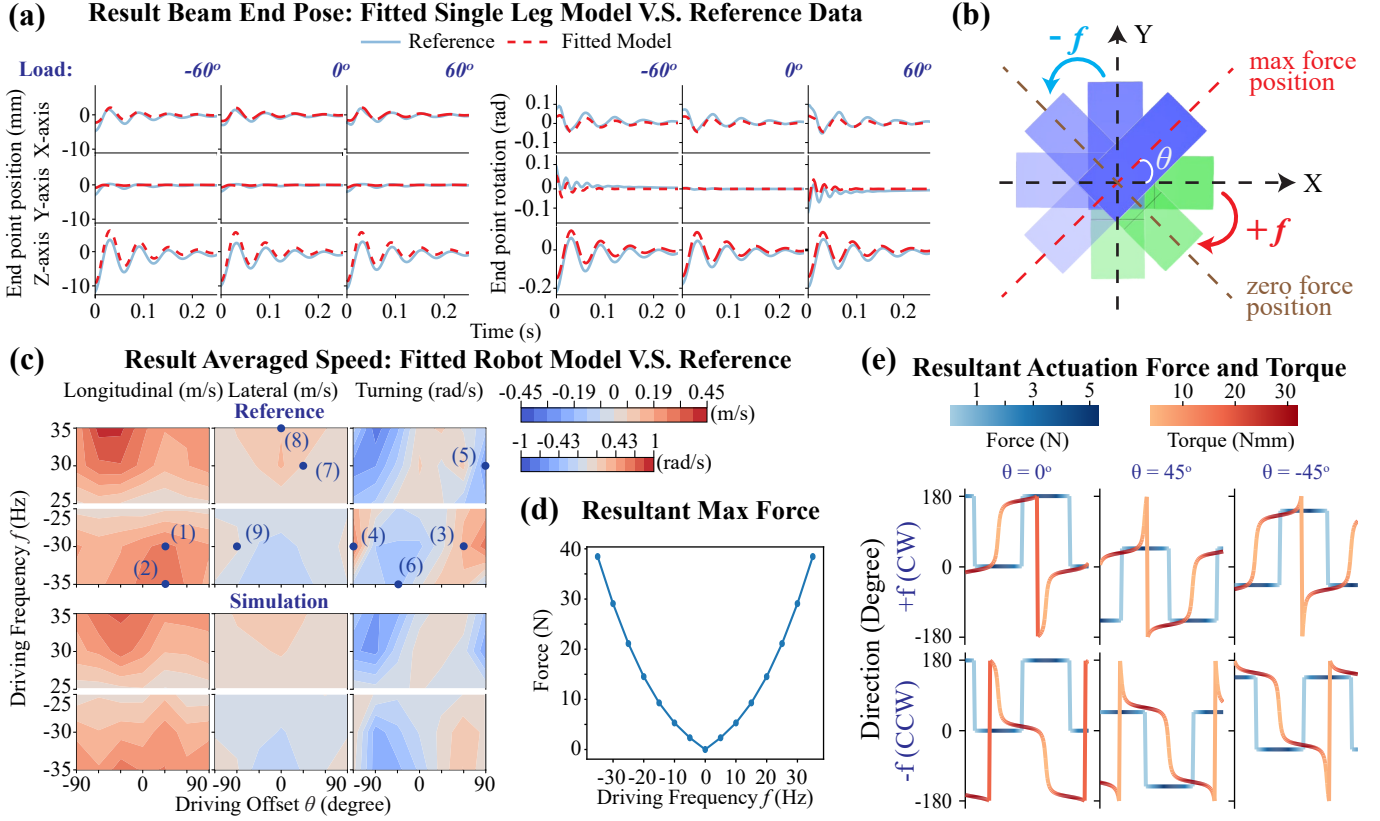


Fig. 3. **Model calibration result and actuation system simulation result.** (a) Single leg model fitting result comparison using end point position and rotation data. (b) Illustration of the actuation system showing its offset angle and driving directions. (c) Comparison of whole-body model fitting results with experimental data from the prototype, using averaged linear velocities in the longitudinal (\bar{v}_x) and lateral directions (\bar{v}_y) and turning velocity ($\bar{\omega}_z$). Index numbers indicate the selected actuation pairs for each locomotion mode (see Section III-A for details). (d) Simulation result: resultant max actuation force v.s. driving frequency. (e) Resultant actuation force and torque for various driving frequencies ($f = \pm 10$ Hz) and offset angles ($\theta = 0^\circ, 45^\circ, -45^\circ$) within one actuation cycle. The Y-axis shows the direction of the resultant force and torque in the X-Y plane, while the color indicates the corresponding magnitude.

opposite directions about a shared axis. The vertical separation between the two offset masses is h . This arrangement produces a consistent shaking force in a single direction while largely canceling out rotational inertia.

As shown in Figure 3(b), the centrifugal forces produced by both masses add constructively along the axis of shared motion and cancel along the orthogonal axis. The angle $\theta \in [-90, 90]^\circ$ defines the offset between the robot's sagittal plane and the direction of maximum force, with positive θ to the right and negative to the left. When $\theta = 0^\circ$, the force is directed along the forward (X) axis; when $\theta = \pm 90^\circ$, it is aligned with the lateral (Y) axis. The driving frequency f sets the rotational speed of the top rotor: positive values correspond to clockwise rotation, negative to counterclockwise. The bottom rotor spins at the same speed but in the opposite direction, effectively minimizing net rotary inertia. The position vectors of the two rotors are:

$$\vec{r}_1(t) = \begin{bmatrix} l \cos(\omega t + \theta) \\ l \sin(\omega t + \theta) \\ h/2 \end{bmatrix}, \quad \vec{r}_2(t) = \begin{bmatrix} l \cos(-\omega t + \theta) \\ l \sin(-\omega t + \theta) \\ -h/2 \end{bmatrix}, \quad (4)$$

where $\omega = 2\pi f$.

The centrifugal force generated by rotor is:

$$\vec{F}_1(t) = m\omega^2 l \begin{bmatrix} \cos(\omega t + \theta) \\ \sin(\omega t + \theta) \\ 0 \end{bmatrix}, \quad \vec{F}_2(t) = m\omega^2 l \begin{bmatrix} \cos(-\omega t + \theta) \\ \sin(-\omega t + \theta) \\ 0 \end{bmatrix}. \quad (5)$$

The resulting net force on the rotor joint, including gravity, is:

$$\begin{aligned} \vec{F}_{\text{total}}(t) &= \vec{F}_1(t) + \vec{F}_2(t) + \vec{F}_g \\ &= 2m\omega^2 l \cos(\omega t) \begin{bmatrix} \cos \theta \\ \sin \theta \\ 0 \end{bmatrix} + 2m \begin{bmatrix} 0 \\ 0 \\ -g \end{bmatrix}. \end{aligned} \quad (6)$$

The net torque on the rotor joint, including gravity, is:

$$\begin{aligned} \vec{\tau}_{\text{total}}(t) &= \vec{r}_1(t) \times [\vec{F}_1(t) - mg\hat{z}] + \vec{r}_2(t) \times [\vec{F}_2(t) - mg\hat{z}] \\ &= \begin{bmatrix} -hm\omega^2 l \sin(\omega t) \cos \theta - 2mgl \cos(\omega t) \sin \theta \\ -hm\omega^2 l \sin(\omega t) \sin \theta + 2mgl \cos(\omega t) \cos \theta \\ 0 \end{bmatrix}, \end{aligned} \quad (7)$$

where \hat{z} represents the unit vector aligned with the Z-axis.

As shown in Eq. 6, the dual-motor system generates the intended unidirectional shaking forces. Although the Z-axis moment is canceled (Eq. 7), a residual shaking torque remains in the X-Y plane, varying with frequency (f) and direction (θ) due to rotor momentum exchange. In practice, this residual torque can manifest as a small systematic yaw bias during

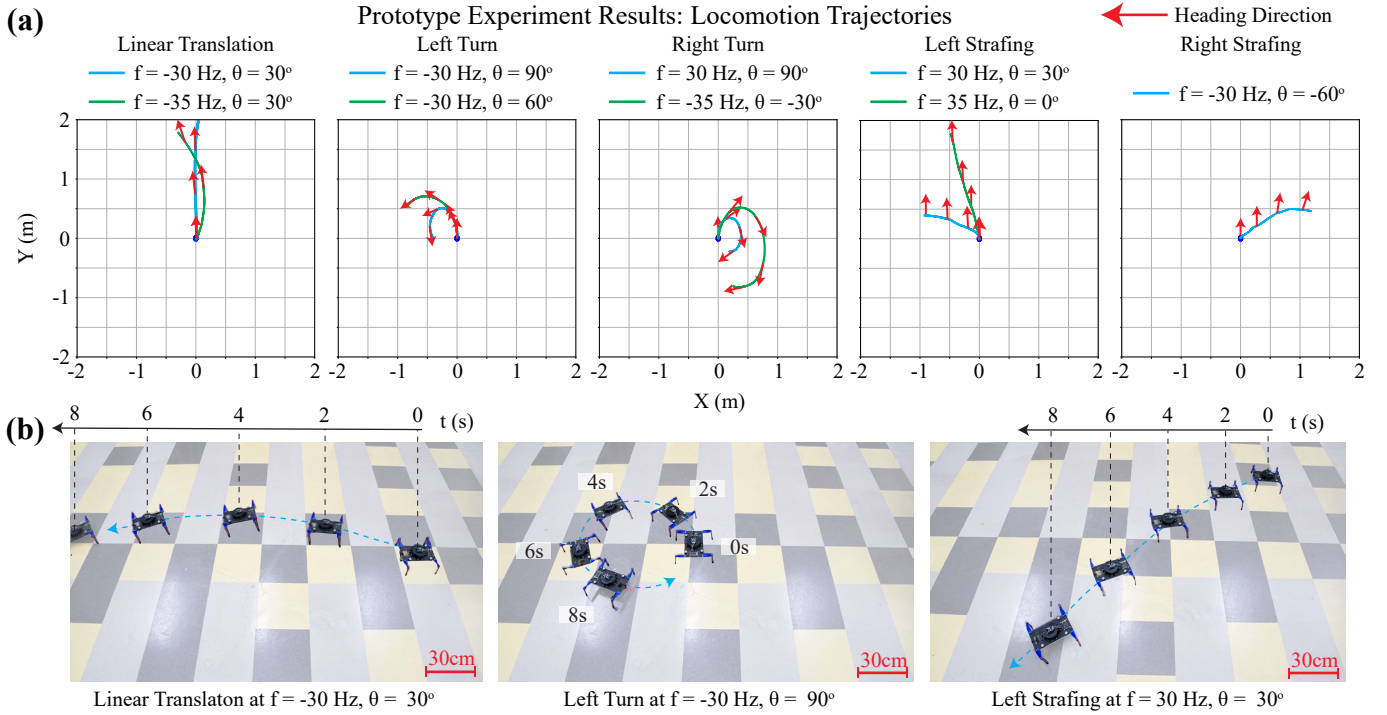


Fig. 4. **Locomotion Analysis** (a) Selected resulting trajectories from prototype experiments demonstrating various locomotion modes; (b) Time-lapse of example locomotion modes (left to right: linear translation, left turn, and left strafing) obtained from the lab experiments.

nominal forward operation, producing gradual veering in open-loop trials. The vertical rotor separation h amplifies this torque, reducing symmetry about the Sagittal and Coronal planes. This dynamic torque causes the asymmetric locomotion seen in the speed profiles of Figure 3(c).

The actuation system is further analyzed in MuJoCo to study the dynamic forces and torques it generates. The simulation setup, shown in Figure 2, closely replicates the prototype using design parameters from Table II. Two rotors are attached to a rotational joint equipped with force and torque sensing. During simulation, the rotors are driven at specified frequencies and offset angles θ , allowing the resulting forces and torques to be recorded.

The directions of the resultant force and torque for driving frequencies $f = \pm 10$ Hz and offset angles $\theta = \{-45, 0, 45\}^\circ$ are presented in Figure 3(e), demonstrating how control inputs produce targeted shaking forces. The results confirm that the actuation system can generate unidirectional shaking forces as intended, with the offset angle θ effectively setting the force direction. Figure 3(d) shows how the maximum shaking force scales with driving frequency. Detailed simulation results are provided in the supplementary video 1.

III. MOBILITY AND SENSITIVITY ANALYSIS

This section first analyzes the experimental data from the prototype to classify the various locomotion modes. Subsequently, we detail the underlying dynamics-based demultiplexing mechanism that allows these specific actuation settings to isolate distinct mobility patterns. Subsequently, we leverage the established simulation as a powerful tool to comprehensively

investigate the system's sensitivities to both internal and external variation factors.

A. Mobility Analysis

We explored how Flix-Walker's different locomotion modes emerge by conducting a series of prototype experiments under various actuation settings. As described in Section II-D and illustrated in Figure 3(b), we systematically mapped each combination of vibration frequency (f) and offset angle (θ) to its resulting locomotion behavior. The experimental trajectories were examined and grouped according to their motion characteristics, as shown in Figure 4(a), summarized in Table III, and highlighted with selected examples in Figure 4(b).

Constrained to planar motion within a 3D space, Flix-Walker possesses three degrees of freedom. When actuated by the shaker, the robot's response blends these degrees of freedom, with the proportions determined by the frequency f and direction θ of the vibration input. As detailed in Table III, each locomotion mode is identified by its dominant velocity component: linear translation by forward speed $|v_x|$, turning by angular speed $|\omega|$, and strafing by lateral speed $|v_y|$. These results show that Flix-Walker's underactuated design can reliably generate a wide range of effective motion patterns using only two actuators.

B. Dynamic Demultiplexing Mechanism

The distinct locomotion modes summarized in Table III arise from "dynamics-based demultiplexing," wherein the same mechanical structure yields different steady motions as the vibration input's frequency and direction are varied.

TABLE III
LOCOMOTION MODE AND MECHANISM ANALYSIS

Locomotion Mode	Freq. f (Hz)	Offset θ ($^\circ$)	Index in Figure 3(c)	Dominant Component
Linear Trans. I	-30	30	(1)	$ v_x $
Linear Trans. II	-35	30	(2)	
Left Turn I	-30	± 90	(3)	$ \omega_z $
Left Turn II	-30	60	(4)	
Right Turn I	30	± 90	(5)	
Right Turn II	-35	-30	(6)	
Left Strafing I	30	30	(7)	$ v_y $
Left Strafing II	35	0	(8)	
Right Strafing	-30	-60	(9)	

The underlying mechanism is the spatial motion conversion inherent to the Soft Twisted Beam geometry: as analytically derived in our prior work [5], the twisted profile mechanically couples planar centrifugal forces (from the eccentric mass in the xy -plane) into vertical bending moments, enabling lift and thrust (xz and yz trajectories) from a purely horizontal input. Leveraging this principle, we synthesize complex, multi-degree-of-freedom gaits. However, because the four compliant twisted legs undergo intermittent ground contact, the global response is nonlinear and hybrid, and is not well represented by a closed-form linear transfer model. We therefore characterize demultiplexing via an empirically identified steady-state input–output mapping from actuation parameters to the time-averaged planar body twist:

$$\mathcal{M} : (f, \theta) \mapsto \bar{\mathbf{V}}(f, \theta), \quad (8)$$

where $\bar{\mathbf{V}} = [\bar{v}_x, \bar{v}_y, \bar{\omega}_z]^T$ is the time-averaged planar body velocity and yaw rate, computed from the body twist $\mathbf{V}(t) = [v_x(t), v_y(t), \omega_z(t)]^T$ over a steady-state window. In practice, \mathcal{M} is obtained from the calibrated simulation and validated experimentally in Figure 3(c), and Table III reports representative operating points.

The mapping \mathcal{M} arises from three coupled effects. First, the direction parameter θ sets the direction of the planar inertial force generated by the shaker (Eq. 6). In addition, the vertical rotor separation h introduces an in-plane residual torque (Eq. 7) whose components depend on θ and whose sign reverses with the rotor spin direction. This asymmetry is crucial for accessing rotational responses. For example, near $\theta = \pm 90^\circ$ the lateral force component is maximized while the forward component is suppressed, and the accompanying residual torque biases asymmetric contact loading, yielding a dominant yaw response ($\bar{\omega}_z$) at the turning operating points in Table III. By contrast, for forward-biased directions such as $\theta = 30^\circ$, the injected force contains a strong longitudinal component, which tends to favor translational motion when the yaw bias from torque and contact asymmetry is small. Second, the frequency f selects the dynamic regime because the effective leg compliance, body–leg coupling, and stick–slip contact rectification are strongly frequency dependent. As a result, even for the same geometric forcing direction θ , changing f can switch which component of $\bar{\mathbf{V}}$ dominates. This effect is visible in the response map (Figure 3(c)) and

explains why operating points with similar θ can produce qualitatively different motions. We intentionally avoid attributing this switching to a simple linear resonance of an isolated leg; rather, it reflects the coupled structure–contact dynamics of the full four-leg system. Finally, the mapping \mathcal{M} is sensitive to parameter variations and disturbances due to the nonlinear structure–contact dynamics. We quantify this sensitivity and introduce a robustness metric in the following sections to identify actuation pairs that yield robust motion modes.

C. Sensitivity Analysis

Our study identifies two major factors that significantly influence Flix-Walker’s locomotion: asymmetric load conditions, and contact friction differences due to terrain conditions. We employ a simulation-based approach using MuJoCo with the model described in Section II-B to analyze actuation parameters, specifically driving frequency and shaking orientation, that are most resilient to these variations. This understanding enables us to identify actuation parameters that consistently and robustly produce motions with minimal variability.

1) *Asymmetric loading condition*: A series of simulations was conducted under asymmetric loading conditions by adding a 50 g payload at different locations on the robot body (front, rear, left, and right), with the payload center located 12 mm away from the robot’s body center along the corresponding direction, as illustrated in Figure 5(g). This load and offset emulate a plausible payload-induced center-of-mass misalignment. We also performed a corresponding prototype test in the lab by attaching a 50 g payload on the left side with the same 12 mm center offset, as shown in Figure 5(f).

We then swept the actuation parameters over $f \in [-35, 35]$ Hz and $\theta \in [-90^\circ, 90^\circ]$. For each (f, θ) pair, we ran an 8 second trial and computed the steady-state time-averaged velocities. The resulting averaged-speed maps are shown in Figure 5(a).

Varying the payload distribution alters the robot’s averaged longitudinal, lateral, and turning responses (Figure 5(a)). In simulation, left/right loading produces the largest deviations: it can create or remove peaks in \bar{v}_x , flip the sign of \bar{v}_y near $\theta = 0^\circ$, and bias the sign of $\bar{\omega}_z$ (e.g., at $(f = -30 \text{ Hz}, \theta = -60^\circ)$). The prototype left-load experiment shows the same qualitative shifts as the corresponding simulated left-load map (Figure 5(a), rightmost column). By contrast, front/rear loading has a smaller effect on \bar{v}_x and \bar{v}_y , while still modulating turning; for instance, it increases $|\bar{\omega}_z|$ near $(f = -35 \text{ Hz}, \theta = -30^\circ)$ and $(f = 35 \text{ Hz}, \theta = 30^\circ)$.

Beyond understanding how loading condition variations affect motion, we aim to identify actuation parameter pairs that yield robust motion outcomes despite these errors. To achieve this, we analyze both the speed deviation and the effectiveness of each actuation pair under mass variations, utilizing an actuation performance index. For each direction, the actuation performance index I is defined as:

$$I = \frac{V_{\text{ref}}}{\text{RMSE}(V_{\text{load}}, V_{\text{ref}})}, \quad (9)$$

where V_{ref} is the reference speed (without asymmetric load), and $\text{RMSE}(V_{\text{load}}, V_{\text{ref}})$ is the root mean squared error between

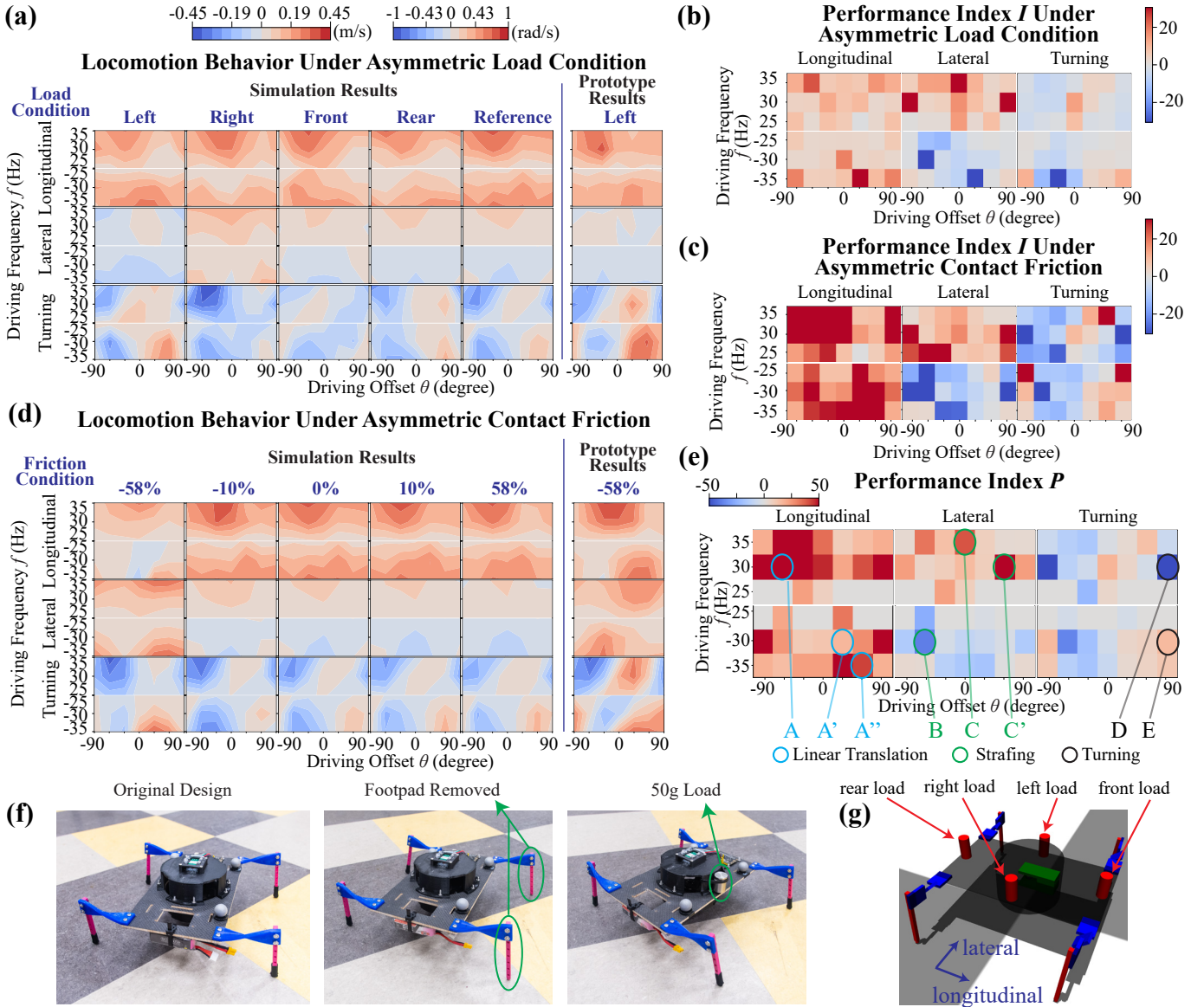


Fig. 5. **Sensitivity analysis using simulation and prototype experiment.** (a) Simulation and prototype experiment results from a 50 g load added to the sides of Flix-Walker. (b) Actuation performance index I under load condition variants; (c) Actuation performance index I under contact friction variants; (d) Simulation and prototype experiment results from asymmetric contact frictions. (e) Actuation robustness index (P) map with selected actuation pairs. (f) Prototype test setup for asymmetric contact friction (middle) and load conditions (right). (g) MuJoCo model for simulation of different load conditions.

the velocities with various mass loading conditions (V_{load}) and the reference. This metric highlights actuation commands (f , θ) that achieve both high speed and resilience to variations in loading conditions. The results of this analysis are shown in Figure 5(b).

2) *Asymmetric contact friction*: Besides variation from mass distribution, contact friction also plays a significant role in Flix-Walker's locomotion. Using the simulation setup in Figure 2, we employ a contact model with two-directional tangential and rolling friction and one-directional twisting friction; tangential friction dominates the motion response. We therefore vary only the tangential friction terms about the calibrated nominal per-leg values $(\mu_{\text{tr}}, \mu_{\text{fl}}, \mu_{\text{rr}}, \mu_{\text{rl}}) = (0.508, 0.646, 0.553, 0.451)$ obtained in Section II-D.

To investigate asymmetric friction, we perturb only the

left-leg tangential coefficients $(\mu_{\text{fl}}, \mu_{\text{rl}})$ by $\pm 10\%$ and $\pm 58\%$. The -58% case models left footpad removal on the prototype, reducing $(\mu_{\text{fl}}, \mu_{\text{rl}})$ from $(0.646, 0.451)$ to $(0.271, 0.189)$ (Figure 5(f), middle). As shown in Figure 5(d), reducing left-side friction amplifies asymmetry in the longitudinal response, biases the turning rate, and induces a lateral drift toward the lower-friction side. Increasing left-side friction produces the opposite trend, shifting the lateral peak direction. We compute the same performance index as in Eq. 9 under friction asymmetries, with results shown in Figure 5(c).

D. Metric for Selecting Actuation Pairs

To identify actuation parameters that achieve the desired motions while remaining robust to variations, we introduce an index P to quantify the overall effectiveness and resilience of

each actuation pair. We first exclude pairs that do not provide sufficient forward locomotion, defined as a heading speed below 0.05 m/s. For the remaining candidates, the actuation performance index P is computed as the average of the summed indices I obtained from the asymmetric loading and the friction analysis. This index yields high values only when both speed is high, and error is low. Figure 5(e) visualizes the results, where darker colors indicate better performance, and red and blue represent the positive and negative direction of the resultant speed, respectively.

TABLE IV
SELECTED ACTUATION PAIRS

Locomotion Mode	Actuation Frequency (f Hz)	Actuation Offset (θ°)	Indices in Figure 5(e)
Linear Translation	-30	30	A'
Left Turn	-30	± 90	E
Right Turn	30	± 90	D
Left Strafing	30	30	C'
Right Strafing	-30	-60	B

Focusing first on linear translation, high longitudinal speed with minimal lateral and turning speeds is prioritized. Based on the metric, three actuation pairs, labeled A , A' , and A'' , are identified as optimal candidates. For strafings, the metric favors high lateral speed with low longitudinal and turning speeds. Accordingly, candidates B , C , and C' are selected: pair B provides a negative Y-direction lateral speed (rightward strafing), while C and C' deliver a positive Y-direction lateral speed (leftward strafing). For turning locomotion, the preferred actuation pairs exhibit high turning speed, lower longitudinal speed, and near-zero lateral speed. Candidates D and E are chosen: pair D provides a negative Z-direction turning speed (rightward turning) with low lateral and favorable longitudinal speeds, while E offers a positive Z-direction turning speed (leftward turning).

IV. WORKING DEMONSTRATIONS

This section presents two untethered closed-loop control demonstrations to illustrate the mobility of Flix-Walker in lab environments. We devised two untethered maneuver tasks using a closed-loop controller with the selected actuation parameters as shown in Table IV.

A. Closed-loop Trajectory Tracking

In this demonstration, we implemented a closed-loop, two-state switching feedback controller utilizing turning control parameters derived from Table IV to achieve an '8'-shaped trajectory tracking task. The outcome is shown in Figure 6. During the experiment, the Flix-Walker operates wirelessly while its position is tracked by an Optitrack system. The robot's pose data is transmitted to a computer, which computes the appropriate control signal and sends it to the robot in real time via WiFi. The controller evaluates the error between the robot's current heading angle and the desired heading, and applies the corresponding control input based on this error.

The trajectory recorded by the Optitrack system is shown in Figure 6(b). It is evident that the robot closely follows the

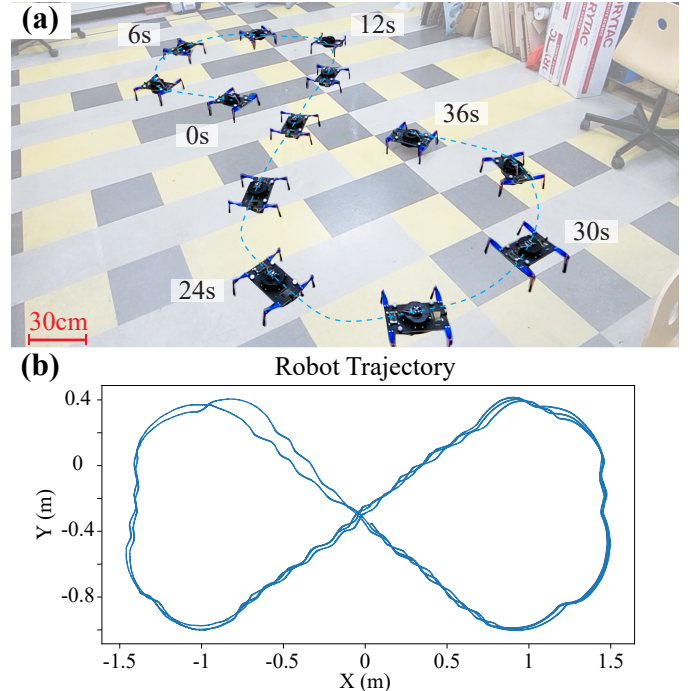


Fig. 6. **Automatic trajectory tracking of a figure '8' pattern.** (a) Time-lapse of the robot trajectory; (b) Robot position data from Optitrack system.

desired path. A recording of this demonstration is available in the supplementary video 2.

B. Autonomous Return-to-Origin under Disturbance

We further demonstrate the self-navigating capability of the Flix-Walker by tasking the robot to autonomously return to a specified origin using the same switching feedback controller. In this demonstration, the robot was intentionally disturbed and pushed away from its original position. Despite these disturbances, the robot effectively navigated back to the origin by relying on the same closed-loop controller. This experiment highlights the robustness of the chosen actuation parameters, as the robot consistently maintains stable locomotion and reliably returns to its starting point, even when perturbed. A video recording of this demonstration is provided in the supplementary video 2.

V. DISCUSSION

This paper presented Flix-Walker, an untethered, lightweight under-actuated quadruped that combines a dual-rotor vibration source with four soft twisted-beam legs to realize controllable 3-DoF planar locomotion. Rather than competing with fully actuated quadrupeds, the contribution is a minimalist soft-robotics platform that leverages embodied dynamics: by varying only the vibration frequency f and direction θ , the same structure produces distinct, repeatable steady motions (forward, lateral, and turning) through an empirically identified mapping $\mathcal{M} : (f, \theta) \mapsto \bar{\mathbf{V}} = [\bar{v}_x, \bar{v}_y, \bar{\omega}_z]^T$. The twisted beams provide the key motion-conversion mechanism (planar inertial excitation to thrust-producing foot trajectories), while the dual-rotor layout enables vectorable forcing and residual in-plane torque that broadens the attainable gait space.

A. Impact

To select robust actuation parameters in this nonlinear hybrid system (compliant legs with intermittent stick–slip contact), we propose a three-step workflow for SCRAM-style robots: (1) build and calibrate a computationally efficient compliant model (PRBM), (2) sweep the actuation domain in simulation to construct a response map, and (3) apply a robustness-oriented metric P to select operating points for experimental validation. Beyond nominal flat-ground tests, prototype experiments under asymmetric contact friction (a measured 58% reduction, $\mu_{\text{left}} = 0.42 \mu_{\text{right}}$) and with an asymmetric 50 g payload show that the selected operating points largely preserve their intended modes, indicating disturbance tolerance. Estimated power (approximately 6 W), CoT (about 5 at $v = 0.35$ m/s), and power-to-weight ratio (17.1 W/kg) provide practical context. Overall, this work is not intended to optimize terrain adaptability or energetic efficiency, but rather to demonstrate how a minimalist, underactuated design can exploit intrinsic dynamics to generate multiple controllable locomotion modes with reduced actuation and system complexity.

B. Limitations

Our approach is rapid and effective for understanding complex compliant systems and selecting useful actuation parameters, but several limitations remain. First, the robot’s design has not been fully optimized. Critical features, such as beam dimensions that strongly influence dynamics, were not tuned, so overall performance may be suboptimal. Second, although both simulation and prototype experiments show that Flix-Walker’s locomotion modes can be selected by adjusting vibration force conditions, the three DoF motions cannot be completely isolated. This arises from the underactuated mapping of 2D actuation forces to 3D motions, which blends dynamic responses across axes. As a result, nominal translational operating points can exhibit small, systematic yaw drift due to unavoidable contact and assembly asymmetries, motivating closed-loop correction. Third, motion is limited by actuator power and the robot’s weight: the available motor, while the optimal in our lab, is still suboptimal and restricts actuation frequencies to below 35 Hz. This constraint reduces the range of behaviors observed experimentally, even though simulations indicate that higher frequencies could unlock additional modes (e.g., backward translation at 100 Hz in simulation, which is not achievable in hardware). Lastly, our modeling emphasizes simple, continuous geometries that pair well with the pseudo-rigid-body model (PRBM) for computational efficiency; more complex shapes may not see the same benefits and would require additional tuning and customization.

VI. CONCLUSION

Flix-Walker demonstrates that an untethered, under-actuated quadruped can achieve controllable 3-DoF planar locomotion by combining a dual-rotor vibration source with compliant twisted-beam legs. The primary conclusion is that *dynamics-based demultiplexing* enables a low-dimensional actuation command (f, θ) to reliably select distinct steady motions, and

that a calibrated PRBM-in-MuJoCo pipeline supports systematic operating-point selection and closed-loop navigation.

Future work will focus on (i) improving model fidelity and generalization by collecting additional calibration data and reducing simulation–hardware mismatch, particularly in contact and parameter variations, (ii) enhancing the actuator/driver bandwidth and power-to-weight ratio to expand the experimentally accessible gait space, (iii) extending autonomy and adaptability through onboard sensing and learning-based or automated decision-making methods for selecting and adapting actuation settings across broader real-world conditions, and (iv) design optimization and scalability studies, including alternative leg geometries, morphology tuning, and system scaling, to examine how mechanical design influences intrinsic dynamics, robustness, and accessible locomotion modes.

REFERENCES

- [1] A. Comoretto, H. A. H. Schomaker, and J. T. B. Overvelde, “Physical synchronization of soft self-oscillating limbs for fast and autonomous locomotion,” *Science*, vol. 388, no. 6747, pp. 610–615, 2025.
- [2] M. Sharifzadeh and D. M. Aukes, “Curvature-induced buckling for flapping-wing vehicles,” *IEEE/ASME Transactions on Mechatronics*, vol. 26, no. 1, pp. 503–514, 2021.
- [3] P. Biswal and P. K. Mohanty, “Development of quadruped walking robots: A review,” *Ain Shams Engineering Journal*, vol. 12, no. 2, pp. 2017–2031, 2021.
- [4] J. Lee, J. Hwangbo, L. Wellhausen, V. Koltun, and M. Hutter, “Learning quadrupedal locomotion over challenging terrain,” *Science Robotics*, vol. 5, no. 47, p. eabc5986, 2020.
- [5] Y. Jiang, F. Chen, and D. M. Aukes, “Tunable dynamic walking via soft twisted beam vibration,” *IEEE Robotics and Automation Letters*, vol. 8, no. 4, pp. 1967–1974, 2023.
- [6] E. Todorov, T. Erez, and Y. Tassa, “Mujoco: A physics engine for model-based control,” in *2012 IEEE/RSJ International Conference on Intelligent Robots and Systems*, 2012, pp. 5026–5033.
- [7] X. Xia, C. M. Spadaccini, and J. R. Greer, “Responsive materials architected in space and time,” *Nature Reviews Materials*, vol. 7, no. 9, pp. 683–701, Jun. 2022.
- [8] P. Jiao, J. Mueller, J. R. Raney, X. Zheng, and A. H. Alavi, “Mechanical metamaterials and beyond,” *Nature Communications*, vol. 14, no. 1, p. 6004, Sep. 2023.
- [9] S. Bonfanti, R. Guerra, F. Font-Clos, D. Rayneau-Kirkhope, and S. Zapperi, “Automatic design of mechanical metamaterial actuators,” *Nature Communications*, vol. 11, no. 1, p. 4162, Aug. 2020.
- [10] X. Zheng, K. Uto, W.-H. Hu, T.-T. Chen, M. Naito, and I. Watanabe, “Reprogrammable flexible mechanical metamaterials,” *Applied Materials Today*, vol. 29, p. 101662, 2022.
- [11] D. Li, S. Huang, Y. Tang, H. Marvi, J. Tao, and D. M. Aukes, “Compliant Fins for Locomotion in Granular Media,” *IEEE Robotics and Automation Letters*, vol. 6, no. 3, pp. 5984–5991, Jul. 2021.
- [12] S. Chopra, D. Vasile, S. Jadhav, M. T. Tolley, and N. Gravish, “Toward Robotic Sensing and Swimming in Granular Environments using Underactuated Appendages,” *Advanced Intelligent Systems*, vol. 5, no. 8, p. 2200404, Aug. 2023.
- [13] M. Hutter, C. Gehring, D. Jud, A. Lauber, C. D. Bellicoso, V. Tsounis, J. Hwangbo, K. Bodie, P. Fankhauser, M. Bloesch, R. Diethelm, S. Bachmann, A. Melzer, and M. Hoepflinger, “AnyMal - a highly mobile and dynamic quadrupedal robot,” in *2016 IEEE/RSJ International Conference on Intelligent Robots and Systems (IROS)*, 2016, pp. 38–44.
- [14] A. Badri-Spröwitz, A. A. Sarvestani, M. Sitti, and M. A. Daley, “Birdbot achieves energy-efficient gait with minimal control using avian-inspired leg clutching,” *Science Robotics*, vol. 7, no. 64, p. eabg4055, 2022.
- [15] A. T. Baisch, O. Ozcan, B. Goldberg, D. Ithier, and R. J. Wood, “High speed locomotion for a quadrupedal microrobot,” *The International Journal of Robotics Research*, vol. 33, no. 8, pp. 1063–1082, 2014.
- [16] J. A. Nyakatura, K. Melo, T. Horvat, K. Karakasiliotis, V. R. Allen, A. Andikfar, E. Andrada, P. Arnold, J. Lauströer, J. R. Hutchinson, M. S. Fischer, and A. J. Ijspeert, “Reverse-engineering the locomotion of a stem amniote,” *Nature*, vol. 565, no. 7739, pp. 351–355, 2019.

- [17] Z. Liu, W. Zhan, X. Liu, Y. Zhu, M. Qi, J. Leng, L. Wei, S. Han, X. Wu, and X. Yan, "A wireless controlled robotic insect with ultrafast untethered running speeds," *Nature Communications*, vol. 15, no. 1, p. 3815, May 2024.
- [18] S. G. Faal, F. Chen, W. Tao, M. Agheli, S. Tasdighikalat, and C. D. Onal, "Hierarchical Kinematic Design of Foldable Hexapedal Locomotion Platforms," *Journal of Mechanisms and Robotics*, vol. 8, no. 1, p. 011005, Feb. 2016.
- [19] D. Feshbach, X. Wu, S. Vasireddy, L. Beardell, B. To, Y. Baryshnikov, and C. Sung, "CurveQuad: A Centimeter-Scale Origami Quadruped that Leverages Curved Creases to Self-Fold and Crawl with One Motor," in *2023 IEEE/RSJ International Conference on Intelligent Robots and Systems (IROS)*. Detroit, MI, USA: IEEE, Oct. 2023, pp. 2485–2492.
- [20] P. A. Bhounsule, J. Cortell, A. Grewal, B. Hendriksen, J. G. D. Karssen, C. Paul, and A. Ruina, "Low-bandwidth reflex-based control for lower power walking: 65 km on a single battery charge," *The International Journal of Robotics Research*, vol. 33, no. 10, pp. 1305–1321, Sep. 2014.
- [21] S. Islam, K. Carter, J. Yim, J. Kyle, S. Bergbreiter, and A. M. Johnson, "Scalable Minimally Actuated Leg Extension Bipedal Walker Based on 3D Passive Dynamics," in *2022 International Conference on Robotics and Automation (ICRA)*. Philadelphia, PA, USA: IEEE, May 2022, pp. 207–213. [Online]. Available: <https://ieeexplore.ieee.org/document/9812053/>
- [22] Y. Jiang, M. Sharifzadeh, and D. M. Aukes, "Reconfigurable soft flexure hinges via pinched tubes," in *2020 IEEE/RSJ International Conference on Intelligent Robots and Systems (IROS)*, 2020, pp. 8843–8850.
- [23] M. Jiang, Q. Yu, and N. Gravish, "Vacuum induced tube pinching enables reconfigurable flexure joints with controllable bend axis and stiffness," in *2021 IEEE 4th International Conference on Soft Robotics (RoboSoft)*, 2021, pp. 315–320.
- [24] Y. Jiang, M. Sharifzadeh, and D. M. Aukes, "Shape change propagation through soft curved materials for dynamically-tuned paddling robots," in *2021 IEEE 4th International Conference on Soft Robotics (RoboSoft)*, 2021, pp. 230–237.
- [25] M. Sharifzadeh, Y. Jiang, and D. M. Aukes, "Reconfigurable curved beams for selectable swimming gaits in an underwater robot," *IEEE Robotics and Automation Letters*, vol. 6, no. 2, pp. 3437–3444, 2021.
- [26] P. Birkmeyer, K. Peterson, and R. S. Fearing, "Dash: A dynamic 16g hexapedal robot," in *2009 IEEE/RSJ International Conference on Intelligent Robots and Systems*, 2009, pp. 2683–2689.
- [27] Y. Zhu, M. Qi, Z. Liu, J. Huang, D. Huang, X. Yan, and L. Lin, "A 5-mm Untethered Crawling Robot via Self-Excited Electrostatic Vibration," *IEEE Transactions on Robotics*, vol. 38, no. 2, pp. 719–730, Apr. 2022.
- [28] L. Tang, C. Wang, S. Ma, Y. Li, and B. Li, "Multidirectional Planar Motion Transmission on a Single-Motor Actuated Robot via Microscopic Galumphing," *Advanced Science*, vol. 11, no. 9, p. 2307738, Mar. 2024.
- [29] M. Rubenstein, C. Ahler, and R. Nagpal, "Kilobot: A low cost scalable robot system for collective behaviors," in *2012 IEEE International Conference on Robotics and Automation*, 2012, pp. 3293–3298.
- [30] T. Li, Z. Zou, G. Mao, X. Yang, Y. Liang, C. Li, S. Qu, Z. Suo, and W. Yang, "Agile and Resilient Insect-Scale Robot," *Soft Robotics*, vol. 6, no. 1, pp. 133–141, Feb. 2019.
- [31] Y. Yan, L. Shui, S. Liu, Z. Liu, and Y. Liu, "Terrain Adaptability and Optimum Contact Stiffness of Vibro-bot with Arrayed Soft Legs," *Soft Robotics*, vol. 9, no. 5, pp. 981–990, Oct. 2022.
- [32] L. L. Howell, A. Midha, and T. W. Norton, "Evaluation of Equivalent Spring Stiffness for Use in a Pseudo-Rigid-Body Model of Large-Deflection Compliant Mechanisms," *Journal of Mechanical Design*, vol. 118, no. 1, pp. 126–131, Mar. 1996.
- [33] A. Cowen-Rivers, W. Lyu, R. Tutunov, Z. Wang, A. Grosnit, R.-R. Griffiths, A. Maravel, J. Hao, J. Wang, J. Peters, and H. Bou Ammar, "Hebo: Pushing the limits of sample-efficient hyperparameter optimization," *Journal of Artificial Intelligence Research*, vol. 74, 07 2022.



Yuhao Jiang received the B.S. degree in mechanical engineering from Donghua University, Shanghai, China, in 2015, the M.S. degree in mechanical engineering from the University of Florida, Gainesville, U.S., in 2017, and the Ph.D. degree in mechanical engineering from Arizona State University, Tempe, U.S., in 2023. He is currently a Postdoctoral Scientist with the Reconfigurable Robotics Lab, EPFL. His research interests include soft robotics modeling and applications, and human-robot interaction.



Fuchen Chen received the B.S. and M.S. degrees in robotics engineering from Worcester Polytechnic Institute, Worcester, MA, USA, in 2017, and the Ph.D. degree in systems engineering from Arizona State University, Mesa, AZ, USA, in 2025. His research interests include origami-inspired and laminate robots.



Jamie Paik received the Ph.D. degree in designing a humanoid arm and hand from Seoul National University, Seoul, South Korea, in 2007. She is currently a Professor at the EPFL, Lausanne, Switzerland, where she is the founder and director of the Reconfigurable Robotics Lab (RRL). Her research interests include soft robotics, reconfigurable robots, origami-inspired mechanisms, and human-robot interaction.



Daniel M. Aukes was a tenured professor in engineering and robotics at Arizona State University before leaving academia. As the director of the IDEALab, he investigated the nexus of design, manufacturing, and data-driven decision-making towards the development of robots that can operate in niche environments, with a focus on affordability and accessibility. Dr. Aukes received his PhD and Masters degrees in Mechanical Engineering from Stanford University, studying the design of underactuated robotics hands. He received his BS in Mechanical Engineering from Northwestern University. Dr. Aukes's industry experiences have focused on manufacturing automation across a wide range of industries including automotive, pharmaceutical, and food-processing.